npj | climate and atmospheric science

www.nature.com/npjclimatsci

ARTICLE OPEN

Check for updates

An analytic model of the tropical cyclone outer size

Shuai Wang[1,2]✉ and Ralf Toumi[1]

There are simple conceptual models of tropical cyclone intensification and potential intensity. However, such a framework has been lacking to describe the evolution of the outer circulation. An analytic growth model of the tropical cyclone outer size is derived from the angular momentum equation. The growth model fits a full-physics idealized tropical cyclone simulation. The lifecycle composite of the best-track outer size growth shows a strong super-linear nature, which supports an exponential growth as predicted by the growth model. The climatology of outer size growth measured by the radius of gale-force wind in the North Atlantic and Eastern Pacific during the period 2004–2017, can be understood in terms of four growth factors of the model: the initial size, the growth duration, the mean growth latitude, and the mean top-of-boundary-layer effective local inflow angle. All four variables are significantly different between the two basins. The observed lifetime maximum size follows a lognormal distribution, which is in line with the law of the proportionate effect of this exponential growth model. The growth model fits the observed outer size well in global basins. The time constant of the exponential size growth is approximately equal to the product of the Coriolis parameter and the mean effective inflow angle above the boundary layer. Further sensitivity experiments with the growth model suggest that the interannual variability of the global lifetime maximum size is largely driven by the variation of growth duration.

npj Climate and Atmospheric Science (2022)5:46 ; https://doi.org/10.1038/s41612-022-00270-6

INTRODUCTION

It has been challenging to quantify the overall destructive potential of landfalling tropical cyclones (TCs). Especially after Hurricane Katrina (2005) and Sandy (2012), more attention has been paid on the impact of TC size at landfall and the development of new destructive metrics for public warning[1–4]. With a similar core intensity, various TC sizes can lead to considerably different destructive potentials[5–7]. After a TC reaches its lifetime maximum intensity, the increase in TC destructive potential can be explained mainly by the expansion of TC size[8,9]. Understanding TC size lifecycle is, therefore, of critical importance.

Tropical cyclone outer size can be defined by the radial extent of near-surface cyclonic circulation with a fixed wind speed[10]. It was found that the outer size in the North Atlantic is significantly smaller than that in the western North Pacific[11] which is the basin with the largest mean outer size globally[12,13]. Outer sizes with different wind speed thresholds may show opposite changes so that when the intensity decays, the high-wind-speed outer radii can shrink and low-wind-speed ones can expand[14]. Wind profile models can provide a more comprehensive picture of the entire low-level wind structure[15–17].

Local environmental conditions influence TC outer size, for example, the synoptic flow patterns in both the upper and lower troposphere[18], relative humidity[19,20], sea-surface temperature[21] and vertical temperature profile[22]. Intuitively the net import of angular momentum from larger radii enhances the local angular momentum and thus the near-surface swirling winds increase[10]. However, it was also found that the outer size may also depend on free-tropospheric air subsidence due to radiative cooling[23].

Despite the substantial amount of research on size climatology, diagnostic wind field models, and environment controls on size, the size evolution itself has received relatively less attention[10,12,24]. Progressive growth of TC outer size after the maturity of intensity was simulated with idealized models[25], which supports a similar finding in the North Atlantic[26]. A recent study[27] reported that: the North Western Pacific typhoons generally grow until the midpoint of their lifetimes whereas the Atlantic hurricanes continue expanding throughout most of their lifecycles (i.e., hurricanes grow for a relatively more extended period than typhoons); hurricanes grow more slowly than typhoons; hurricanes have a smaller initial size at genesis than typhoons; and hurricanes exhibit a smaller lifetime maximum size (LMS) than typhoons. These findings were however only based on reanalysis and climate model data.

In this study, we will use the radius of gale-force wind (R_{34}, 34 kt ≈ 17.5 m s^{-1}) from the TC best track data set for the analysis of outer size growth. The period of interest in a TC lifecycle is from the first time when R_{34} starts to be recorded in at least one quadrant in the best track, to the time when the quadrant averaged R_{34} reaches its lifetime maximum for the first time.

The objectives of this study include: formulating the first growth model of TC outer size; validating the derived exponential model for TC size growth with idealized simulations and observations; comparing the climatology of key growth factors between the North Atlantic (NA) and Eastern Pacific (EP) TCs; exploring the physical reasons for the difference in the LMS climatology between the NA, EP and other basins; and investigating the driving factors for the interannual variability of the global LMS.

RESULTS

Variable definition and assumptions

The growth model is derived for a wind radius that is larger than the radius of maximum wind speed in an axisymmetric cylindrical coordinate. We first define the variables used in the derivation at the top of the boundary layer in Table 1. There are numerous definitions and methods for defining the top of the boundary layer[28]. Since the growth model will be derived from the momentum equation the dynamical boundary layer height, i.e., the heights of the maximum wind speed varying with radius, is applied in this study to define the top of the boundary layer. The model is established on the assumption that at the top of a TC

[1]Department of Physics, Imperial College London, London SW7 2AZ, UK. [2]Program in Atmospheric and Oceanic Sciences, Princeton University, Princeton, NJ 08540-6654, USA. ✉email: shuai.wang@princeton.edu

Table 1. Variable definition.

r	Radius
t	Time
z	Height
f_o	The Coriolis parameter
V_t	A fixed tangential wind speed
R_V	Outer wind radius of V_t
M_V	Absolute angular momentum per unit mass at R_V and V_t
w_V	Vertical velocity at R_V and V_t
F_V	Diffusion at R_V and V_t
V_r	Radial velocity at R_V and V_t (define $V_r > 0$ as radial inflow)
a_V	Effective inflow angle[44] defined as $\tan a_V = V_r/V_t$ at R_V and V_t
$\overline{a_V}$	Mean effective inflow angle defined as the mean of a_V during one growth event of R_V
V_m	Maximum wind speed
R_m	Radius of V_m

boundary layer the flow is in gradient wind balance and therefore a_V is small and temporally quasi-stationary at R_V where V_t is fixed.

With flight observations, the TC tangential wind above the boundary layer has been shown in gradient wind balance to a good approximation[29]. Considering the radial momentum equation in the free atmosphere, a gradient wind balance assumes a small radial velocity maintaining a quasi-steady state, i.e., $\partial V_r/\partial t \approx 0$. This approximation applies at the top of the boundary layer during the growth time of an outer size R_V that is away from the eyewall. A physically plausible mean effective inflow angle $\overline{a_V}$ during the growth can be therefore hypothesized. Note that $\partial a_V/\partial t \approx 0$ assumes a_V following a fixed tangential wind V_t at R_V is quasi-stationary during the growth phase in the outer rainbands, and only has high-frequency fluctuations around its mean value $\overline{a_V}$ during the growth of R_V. $\overline{a_V}$ can vary from storm to storm. We will further justify this inference with idealized TC simulations. In addition, the Coriolis parameter is treated as a time-invariant variable for each cyclone and calculated as the mean latitude during the growth of each TC.

An exponential growth model for tropical cyclone outer size

The growth model is derived in an axisymmetric framework. The angular momentum at R_V can be written as

$$M_V = V_t R_V + \frac{1}{2} f_o {R_V}^2. \tag{1}$$

The angular momentum budget at R_V is then given at the top of the boundary layer by

$$\frac{\partial M_V}{\partial t} - V_r \frac{\partial M_V}{\partial r} + w \frac{\partial M_V}{\partial z} + rF_V = 0. \tag{2}$$

The four terms in Eq. (2) represent the local rate of change, radial momentum flux, vertical momentum flux, and the impact of diffusion.

By substituting Eq. (1) in the first two terms, Eq. (2) can be rearranged as

$$\begin{aligned} R_V \tfrac{\partial V_t}{\partial t} + V_t \tfrac{\partial R_V}{\partial t} + \tfrac{1}{2} f_o \tfrac{\partial \left({R_V}^2\right)}{\partial t} &= V_r R_V \tfrac{\partial V_t}{\partial r} + V_t V_r \tfrac{\partial R_V}{\partial r} \\ &+ \tfrac{1}{2} f_o V_r \tfrac{\partial \left({R_V}^2\right)}{\partial r} - w \tfrac{\partial M_V}{\partial z} - rF_V. \end{aligned} \tag{3}$$

We next apply Eq. (3) following R_V rather than the air parcel and this approach has also been recently used to study the eyewall contraction and rapid intensification[30]. Such a change requires a coordinate transformation from (r, z, t) to $(R_V(t), z, t)$ for Eq. (3). This transformation changes the term $R_V \frac{\partial V_t}{\partial t}$ in coordinate (r, z, t) to $R_V(\frac{\partial V_t}{\partial t} + \frac{\partial V_t}{\partial R_V}\frac{\partial R_V}{\partial t})$ in coordinate $(R_V(t), z, t)$, and also replaces the coordinate r to R_V. Note that the transformation above can not be applied to terms containing $\frac{\partial R_V}{\partial t}$ or $\frac{\partial {R_V}^2}{\partial t}$, otherwise one would obtain incorrect relations, e.g., $\frac{\partial R_V}{\partial t}$ in coordinate (r, z, t) to $\frac{\partial R_V}{\partial t} + \frac{\partial R_V}{\partial R_V}\frac{\partial R_V}{\partial t} = 2\frac{\partial R_V}{\partial t}$ in coordinate $(R_V(t), z, t)$.

The terms affected by the coordinate transformation can be written as follows:

$$\begin{aligned} (r, z, t) &\rightarrow (R_V(t), z, t) \\ R_V \tfrac{\partial V_t}{\partial t} &\rightarrow R_V \tfrac{\partial V_t}{\partial t} + R_V \tfrac{\partial V_t}{\partial R_V}\tfrac{\partial R_V}{\partial t}, \\ V_r R_V \tfrac{\partial V_t}{\partial r} &\rightarrow V_r R_V \tfrac{\partial V_t}{\partial R_V}, \\ V_t V_r \tfrac{\partial R_V}{\partial r} &\rightarrow V_t V_r, \\ \tfrac{1}{2} f_o V_r \tfrac{\partial \left({R_V}^2\right)}{\partial r} &\rightarrow f_o V_r R_V. \end{aligned}$$

By applying the coordinate transformation above, Eq. (3) can be rewritten as

$$\begin{aligned} &R_V \tfrac{\partial V_t}{\partial t} + R_V \tfrac{\partial V_t}{\partial R_V}\tfrac{\partial R_V}{\partial t} + V_t \tfrac{\partial R_V}{\partial t} + \tfrac{1}{2} f_o \tfrac{\partial \left({R_V}^2\right)}{\partial t} \\ &= V_r R_V \tfrac{\partial V_t}{\partial R_V} + V_t V_r + f_o V_r R_V - w \tfrac{\partial M_V}{\partial z} - rF_V. \end{aligned} \tag{4}$$

We next conduct scale analysis for Eq. (4). The variable V_t is a fixed wind speed used to define the outer wind radius R_V, so $\frac{\partial V_t}{\partial t} = 0$ by definition. The angular momentum tendency will therefore be caused by changes in the radius. However, the radial gradient of tangential wind, $\frac{\partial V_t}{\partial R_V}$, should vary with the growth of R_V. To estimate the scale of $\frac{\partial V_t}{\partial R_V}$, we use the modified Rankine Vortex[15] at R_V considering its simple expression and good ability to present the outer wind profile[31]. The modified Rankine Vortex can be written at R_V as

$$V_t = V_m \left(\frac{R_V}{R_m}\right)^x, R_V > R_m. \tag{5}$$

Now the radial gradient of tangential wind, $\frac{\partial V_t}{\partial R_V}$, can be estimated with

$$\frac{\partial V_t}{\partial R_V} = V_m R_m^{-x} x R_V^{x-1}. \tag{6}$$

By taking the typical values of $x = -0.5$ (ref. [31]), 50 m s^{-1} for V_m, 50 km for R_m and 250 km for R_V into Eq. (6) we find a typical scale of 10^{-5} for $\frac{\partial V_t}{\partial R_V}$.

For the other terms, since the growth model is developed for TC outer size, the scales of all quantities at the top of the boundary layer are estimated within the radial distance of about 100–500 km from TC centre, which covers the typical values of, for example, the radii of 18 and 12 m s^{-1} at surface[12,13]. Within this radial range, the height of the boundary layer is about 1000–1500 m (ref. [28]). By considering the scales found in previous studies as shown in Table 2, the magnitudes of the terms in Eq. (4) are:

$$\begin{aligned} R_V \tfrac{\partial V_t}{\partial R_V}\tfrac{\partial R_V}{\partial t} &\sim 10^0 \\ V_t \tfrac{\partial R_V}{\partial t} &\sim 10^1, \\ \tfrac{1}{2} f_o \tfrac{\partial \left({R_V}^2\right)}{\partial t} &\sim 10^0, \\ V_r R_V \tfrac{\partial V_t}{\partial R_V} &\sim 10^0, \\ V_t V_r &\sim 10^1, \\ f_o V_r R_V &\sim 10^1, \\ w \tfrac{\partial M_V}{\partial z} &\sim 10^0, \\ rF_V &\sim 10^0. \end{aligned}$$

Scale analysis now suggests that Eq. (4) may be simplified and rearranged as

$$\frac{dR_V}{dt} = V_r + f_o R_V \tan \alpha_V, \tag{7}$$

where $\tan \alpha_V = V_r/V_t$ is used as previously defined. The term $\partial R_V/\partial t$ on the l.h.s. is the evolution of an outer size defined by a fixed tangential wind speed, V_t.

We next apply (1) the assumption given in the last sub-section to replace the time-dependent α_V with its mean value $\overline{\alpha_V}$ (time-invariant) during the growth and (2) the small-angle approximation $V_r/V_t \approx \tan \overline{\alpha_V} \approx \overline{\alpha_V}$ (according to the scales in Table 2) and then obtain

$$\frac{dR_V}{dt} = V_t \overline{\alpha_V} + f_o R_V \overline{\alpha_V}. \tag{8}$$

Now in Eq. (8), R_V is the only time-dependent variable. Integrating Eq. (8) with an initial condition of $R_V = R_o$ at $t = 0$ results in

$$R_V = \left(\frac{V_t}{f_o} + R_o\right) e^{(f_o \overline{\alpha_V})t} - \frac{V_t}{f_o}. \tag{9}$$

Equation (9) is the full expression of a new analytic solution for TC outer size growth. The derived model depicts an exponential growth with a time constant of $f_o\overline{\alpha_V}$. It is noteworthy that V_t/f_o is a hypothetical radius for V_t when the Rossby number is unity. It can also be regarded as to a inverse-f scale when V_t is replaced by the maximum potential intensity, which has dynamical scaling implications for TC size in rotating radiative-convective equilibrium simulations and aqua-planet frameworks[32]. The derived growth model suggests that the TC outer size growth is primarily dominated by four factors:

- initial size.
- growth duration.
- mean latitude during growth.
- mean effective inflow angle at the top of boundary layer.

The doubling time is a useful concept to quantify an exponential growth process. Assuming that it takes a TC time T_D to grow from R_o to $2R_o$, the doubling time of Eq. (9) is then given by:

$$T_D = \frac{ln\left(1 + \frac{f_o R_o}{f_o R_o + V_t}\right)}{f_o \overline{\alpha_V}}. \tag{10}$$

Figure 1a shows the fit of the growth model (Eq. (9)) to the outer size (R_{34}) evolution in the full-physics simulation (see "Methods" for the growth model fit and idealized simulation set-up). The growth model fully captures the simulated outer size growth ($r = 0.99$, P value < 0.01). From the fit we infer a mean effective inflow angle $\overline{\alpha_V}$ of 1.0° at the top of the boundary layer. Figure 1b shows that this mean effective inflow angle is seen in the simulation at a height of about 1500 m above the surface R_{34}. Therefore, the assumptions for the inflow angle required for the analytic growth model are well-validated by the full-physics simulation. The inflow angle at the top of the boundary layer is therefore excellently predicted by the analytic model. We do not find a statistically significant (P value > 0.05) change of the inflow angle during the growth period in this simulation, which justifies the steady-state assumption of V_r (i.e., $\partial V_r/\partial t \approx 0$) and applying a mean effective inflow angle $\overline{\alpha_V}$ in one growth event (from Eqs. (7) to (8)). At this height, the mean wind adjustment factor at R_{34} is found to be 0.76 in the simulation, which is very close to 0.75, the value assumed for the R_{34} growth fit (see "Methods").

Table 2. Characteristic values of the quantities related to Eq. (4).

Quantity	Scale	Source
R_V	10^5 m	By definition
V_t	10^1 m s^{-1}	Ref. [28]
V_r	10^0 m s^{-1}	Ref. [28]
$w\frac{\partial M_V}{\partial z}$	10^0 m^2 s^{-2}	Ref. [70]
rF_V	10^0 m^2 s^{-2}	Ref. [70]
f_o	10^{-4} s^{-1}	As observed in Table 3
Δt	10^5 s	As observed in Table 3
$\frac{\partial V_t}{\partial R_V}$	10^{-5} m s^{-2}	Modified Rankine vortex[15]

Based on the typical values of f_o and R_V, the scales of $\frac{1}{2}f_o$, ΔR_V and $\Delta R_V{}^2$ are estimated to be 10^{-5}, 10^5 and 10^{10}, respectively.

Observations

We next validate the growth model by compositing the TC outer size to paint a general picture for the observed outer size evolution. Figure 2 shows that on average the TC outer size increases in the NA and EP in a super linear fashion within at least the last 2 days before reaching the LMS. The absolute change of

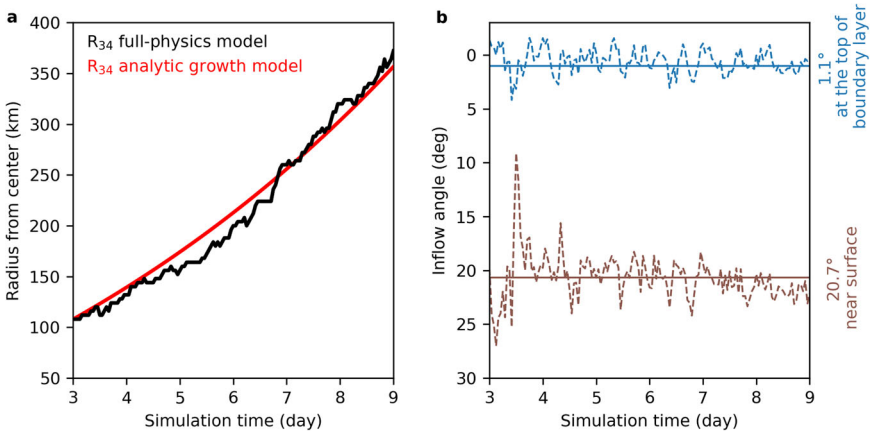

Fig. 1 Time series of outer size and inflow angle in the full-physics idealized model. a The growth of outer size (R_{34}) at a height of 10 m (black line) and the best fit with the growth model (red line). A wind reduction factor of 0.75 is applied (see "Methods"). **b** Time series of inflow angles at the lowest model level (brown dashed line) and the top of the boundary layer (blue dashed line) following the growing R_{34} in (**a**). The inflow angles are calculated based on the azimuthally averaged tangential and radial winds. The solid lines show the mean inflow angles. The mean effective inflow angle during this growth event is estimated to be 1.1° at the top of the boundary layer.

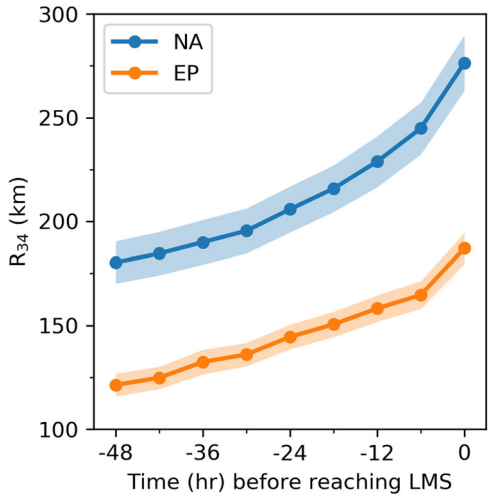

Fig. 2 Composite of R_{34} for 48 h before NA and EP TCs reach the LMS at time 0. The solid lines show the mean evolution and the shading areas denote one standard error to the mean. The composites are based on 6-h observations (dots). There are 94 and 107 TCs used in the NA and EP, respectively.

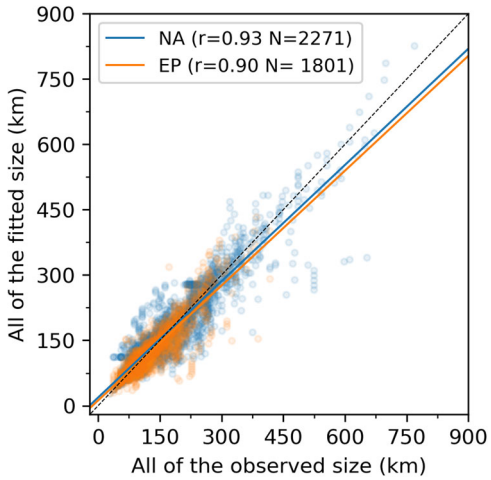

Fig. 3 Comparison between the observed R_{34} in the best track and the correspondingly fitted values of NA and EP TCs. The solid line denotes the linear least-squares fit. The dotted line shows the $y = x$ line. The r values in the legend are the Pearson correlation coefficient with the total number (N) of size observations.

size for every 6 h increases when approaching the LMS. This is qualitatively in line with the prediction by the exponential growth model.

We next continue the quantitative validation of the growth model by fitting individual TC outer size growth in the NA and EP. The three inputs—i.e., the initial size R_o, growth duration t, and the Coriolis parameter f_o calculated with the mean latitude during a growth—are taken from the best-track data. The mean effective inflow angle $\overline{\alpha_V}$ is treated as a fitting parameter for each TC (see "Methods"). Figure 3 shows that the Pearson correlation coefficient between all fitted and observed R_{34} is 0.93 and 0.90 in the NA and EP, respectively, with a slope of 0.89 and 0.86. Partial correlation analysis reveals that correlation coefficient in Fig. 3 does not change if the mean f_o is used for all TCs, and only changes in the NA from 0.93 to 0.91 if the mean R_o is adopted. The results in Figs. 2 and 3 suggest that the exponential growth model is a plausible choice to describe the TC outer size growth. The slopes, less than one in Fig. 3, suggest that the growth model may underestimate the size growth when approaching the LMS.

Difference between basins

The growth model suggests that the following factors can depict a TC growth:

1. Lifetime maximum size,
2. Initial size,
3. Growth duration,
4. Mean growth latitude, and
5. Mean Effective inflow angle.

We next conduct inter-basin comparisons of factors (1)–(4) with the best-track data, and factor (5) based on the estimates from fits (see "Methods").

Figure 4a displays the probability density function (PDF) of the log-transformed LMS in the NA and EP. According to the Kolmogorov–Smirnov (KS) test statistics, the P value from the normality test of the transformed LMS distributions is 0.45 and 0.62, respectively, for NA and EP TCs. This means the distribution of LMS in these two basins has a strong lognormal feature.

Figure 4b shows the log-transformed distribution of initially recorded R_{34}. The mean TC intensity at the time when the initial R_{34} is measured is 36 kt for both NA and EP TCs. Compared to the distribution of LMS, the log-transformed initial size is still somewhat skewed (Fig. 4b), but the P value of a normality test is 0.10 in the NA and 0.01 in the EP, respectively. This suggests a much weaker lognormal feature of the initial size than the LMS in both basins. Figure 4a and b suggests that the exponential growth process enhances the lognormality of the outer size distribution when growing towards the LMS. We will further discuss this point in the next section.

The growth duration, as shown in Fig. 4c, is defined as the growth period from the initial size to LMS. Positive skewness is found in both basins. A longer growth duration (Fig. 4c) and higher mean growth latitude (Fig. 4d) are found in the NA but they are not significantly correlated.

More quantitative comparison of the growth factors is summarized in Table 3. The statistical significance of the differences between the two basins are also examined by bootstrapping (see "Methods"). The observed LMS in the best track and estimated LMS from the fit show consistent differences between the two basins. Compared to the EP, an NA TC typically has a larger initial size, grows for a longer period at a higher mean latitude, and ends with a larger LMS. The LMS, initial size, growth duration, and mean latitude between the two basins are significantly different at the 99% confidence interval.

The TCs in the EP have a significantly larger inflow angle than NA TCs (P value = 0.04, Table 3). However, the doubling time, which is a measure of relative growth rate, is not significantly different between the two basins. This may be because the larger inflow angle in the EP is compensated by a lower mean growth latitude. According to the growth model, a larger LMS in the NA is then determined by a larger initial size and a longer growth duration, given the doubling time is similar in the two basins.

The analytic model in other basins

It is of interest to also validate the growth model in the other basins. Table 4 shows the Pearson correlation coefficient together with the associated P value from the least-squared linear fit between the observed and fitted TC size. The global correlation coefficient is 0.83, with variation between 0.80 and 0.87 in all the basins, and the corresponding P value is consistently less than 0.05. The mean root-mean-square error of the global TCs is 24 km, and this is 15% of the global mean R_{34} (157 km). The root-mean-square error varies from 14 to 27 km in all the basins.

Since the model can in general depict the TC outer size growth globally, we next investigate the global model features: the LMS,

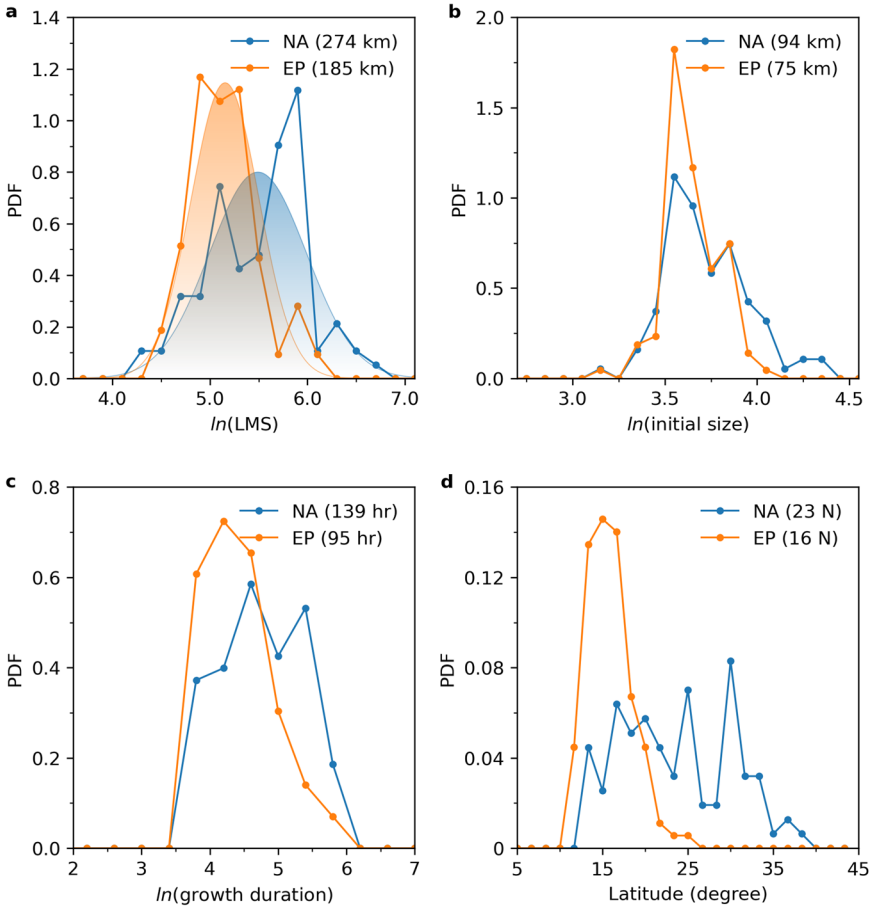

Fig. 4 Distribution of TC growth factors. PDF of log-transformed (**a**) LMS (km), (**b**) initial size (km), (**c**) growth duration (h), and (**d**) mean growth latitude (°N) for NA and EP TCs. The solid lines and dots are the observed PDFs based on the best track. The bell-shaped shadings in (**a**) denote the fitted normal distribution. The *P* value from the lognormal test of LMS is 0.45 in the NA and 0.62 in the EP, respectively, which suggests that the distributions are lognormal. The bin widths are 0.2 in (**a**), 0.2 in (**b**), 0.4 in (**c**), and 2° in (**d**). The mean in each basin is given in the legend.

Table 3. Statistics of the growth factors.

		NA	EP	*P* value
Inputs	Initial size (km)	94 [46,179]	75 [46,116]	<0.01
Inputs	Duration (h)	139 [48,282]	95 [44,230]	<0.01
Inputs	Latitude (°N)	23 [14, 33]	16 [12, 20]	<0.01
Estimates	Inflow angle (degree)	0.7 [0.1,0.9]	0.9 [0.1,2.2]	0.04
Estimates	Doubling time (h)	90 [26,237]	92 [23,293]	>0.1
Estimates	Lifetime maximum size (LMS, km)	247 [92,496]	178 [93,329]	<0.01
	Observed LMS (km)	274 [108,586]	185 [111,348]	<0.01

Mean of the six parameters (three inputs and three estimates, see "Methods") from the fit of the growth model to the best-track size evolution in the NA (94 TCs) and EP (107 TCs). The observed lifetime maximum size is also given for comparison. The range of the 5th and 95th percentiles are provided in square brackets. The *P* value shows the statistical significance of the inter-basin difference based on bootstrapping.

Table 4. Validation of the growth model by fitting to the size growth of individual storms globally.

	Global	NA	EP	WP	NI	SI	SP
r	0.83	0.81	0.82	0.85	0.87	0.82	0.80
P value	0.02	0.03	0.03	0.02	0.03	0.02	0.03
RMSE (km)	24	27	18	27	14	23	27
TC number	549	94	107	198	23	84	43

The Pearson correlation coefficient *r*, *P* value and root-mean-square error (RMSE) are the mean of all fittings in each basin and globally. The *P* value is two-sided with a null hypothesis that the slope is zero using Wald test with t-distribution.

initial size, growth duration, mean growth latitude, mean effective inflow angle following R_{34}, and doubling time (Table 5). The inter-basin differences of these variables are also examined by testing the statistical significance of a variable's distribution in each basin (BASIN) against that in all the other basins (ex-BASINs). If one variable, according to bootstrapping, shows a significant difference between one pair of BASIN and ex-BASINs, it indicates the particularity of this variable in BASIN.

Each basin, apart from the SI and SP, have significantly different mean LMS compared to the rest of the basins (Table 5). NA and WP TCs show larger LMS, whereas the LMS in the EP and NI are generally smaller. There are different reasons for the uniqueness of LMS in these basins and it can be usefully understood in terms of the growth model. The NA has a significantly longer growth duration at a higher mean latitude, whereas the WP has

Table 5. Mean growth factors of global TCs.

	Global	NA	EP	WP	NI	SI	SP
LMS (km)	241	274+	185−	268+	184−	231	239
Initial size (km)	90	94	75−	95+	83	93	93
Duration (h)	100	139+	95	95	63−	87−	97
Latitude (°N/S)	18	23+	16−	19	14−	16−	16−
Inflow angle (°)	1.0	0.7−	0.8−	1.1+	1.1	1.1	1.0
Doubling time (h)	77	90 +	92+	69	61	71	71

The LMS, initial size, growth duration, and mean latitude during growth are calculated with the best-track data. The inflow angle and doubling time are obtained as the fitting estimates (as in Table 3). The storm events in each basin are compared to the events in the other basins. If a quantity in one basin is significantly larger or smaller than the mean in the other basins at 95% confidence interval, it is indicated with a "+" or "−" sign.

significantly larger initial size and mean effective inflow angle. The anomalously small LMS in the EP is mainly due to the small initial size and mean effective inflow angle at a lower mean latitude during growth. In the NI the short growth duration at a lower mean latitude leads to a small LMS. All basins have unique combinations of initial size, mean growth latitude and/or mean effective inflow angle. These three factors determine the doubling time (Eq. (10)). The NA and EP have significantly longer doubling time than in the other basins. This is likely due to a smaller mean effective inflow angle as this is the only growth factor in the NA and EP that is different compared to that in the other basins.

Interannual variation of the LMS

The growth model identifies four factors for TC size growth: the initial size, growth latitude, local effective inflow angle, and growth duration. This provides a simple way to understand the interannual variation of the LMS. In this section, we focus on the medians of the LMS and growth factors considering their skewness. We do not find any significant trend of the observed annual median LMS (Fig. 5). With the observed four factors of each TC, the model can reproduce the interannual variation of the LMS in a good agreement with the observation. The correlation between the modeled and observed annual LMS time series is 0.86 after detrending (Fig. 5a). We next perform sensitivity experiments by fixing each of the four growth factors to their global medians to examine their relative importance by comparing the correlation between the observed and modeled LMS time series. The growth latitude is found to contribute little to the interannual LMS variation (Fig. 5b). The growth duration and initial size (Fig. 5c, d) show a relatively large influence. However, if the initial size is fixed, the modeled and observed LMS shows an almost perfect synchronous change for some of the period (2004–2013), which does not happen when the growth duration is fixed. This suggests that the growth duration may be the most important and consistent growth factor to the interannual variation of the LMS. The effective inflow angle is relatively less important to the interannual variation, but it does seem to be crucial to push up the modeled LMS to the observed level (Fig. 5b).

DISCUSSION

There are simple and useful analytic models for TC intensity change[33–35]. A simple analytic model for TC outer size growth has been lacking. Here we present a growth model developed explicitly for the TC outer size, which can be used to understand the inter-basin difference of the LMS and its interannual variation. The model also explains several empirical findings into a single framework:

- that the initial size is important[36];
- that TC size increases with latitude[26];
- the inter-basin differences of size[13]; and
- that the TC outer size is log-normally distributed[37].

The growth model is developed for TC outer circulation, a regime that has different dynamics from the inner-core region where the radius of maximum wind is located[17]. In particular, the vertical advection and diffusion are much less important at the outer circulation than in the eyewall. The growth model suggests that the TC outer size growth is primarily dominated by four factors: the initial size, growth duration, mean growth latitude, and mean effective inflow angle. Numerical studies of idealized TCs showed that an initially large TC is more likely to reach a large size at a later stage[38,39]. According to our analysis, WP TCs have both significantly larger initial size and LMS, which supports those idealized simulations. However, the growth model also suggests that the growth duration, mean effective inflow angle and latitude determine the lifetime maximum size for the same initial size. It has been shown that the duration of major tropical cyclones for 1982–2018 has been shortened by 1 day[40]. If we assume the same reduction for the mean growth duration, with the global mean values of $R_o = 90$ km, latitude=18°N/S, $\overline{\alpha_V} = 1.0^\circ$ and duration = 100 h (Table 5), the growth model predicts a reduction of mean LMS by −53 km over 37 years, i.e., −1.4 km per year. This predicted change is close to an observed value in a recent study[41] showing that the global annual mean R_{34} (not LMS shown in Fig. 5) is decreasing with a rate of −2.5 km per year based on best-track data. However, no changes of size based on satellite observations have been reported[26]. Our results also reveal that the LMS does not show a significant change, which is consistent with a steady annual mean R_{34} inferred from ocean cold wakes[42]. Poleward migration of TC lifetime maximum intensity has been found in recent decades[43]. However, further analysis (not shown) reveals that the growth model is the least sensitive to any latitude change compared to the other growth factors. For example, the LMS would only increase by less than 10% if the growth latitude were to increase by 50% with other factors fixed.

The inflow angle is of crucial importance in our growth model. However, there has been a lack of studies on the inflow angle at the top of the boundary layer in the outer-core region. A previous study[28] finds a boundary layer depth at surface R_{34} is about 1400 m, with $V_t = 31$ m s^{-1}, and $V_r = 1$ m s^{-1} at this height, which gives an inflow angle of about 1.8° (their Fig. 4). The magnitude of this inferred top-of-boundary-layer inflow angle agrees with our estimates from simulations (1.0°) and observations (also 1.0° globally). It should be noted that the concept of inflow angle in this study is assumed to be axisymmetric. However, for any given time and storm this inflow angle could be asymmetric because of, for example, storm motion and shear[44].

Based on flight-level datasets, two primary types of growth processes were previously suggested[45]: an internally dominated process relating to secondary eyewall formation and eyewall replacement cycles, and an externally forced process by the synoptic environment. Environmental and internal conditions that have been found to be important to the TC outer size change, e.g., the potential intensity and midlevel relative humidity[46], the surface fluxes[47], the dynamics in the boundary layer[48], and convective processes[49,50], are not directly included in the derived growth model. However, the inflow angle can be taken as a key physical variable linking the effects of internal and external conditions and then directly affecting the growth process (as shown by Eq. (8)). A further opportunity, beyond the scope of this work, may be to establish statistical relationships between the inflow angle and real-time internal and environmental conditions.

The proposed growth model does not predict a maximum equilibrium R_{34} (if there is one per se). This is different from other TC intensification models[33,34]. Considering the differential form of

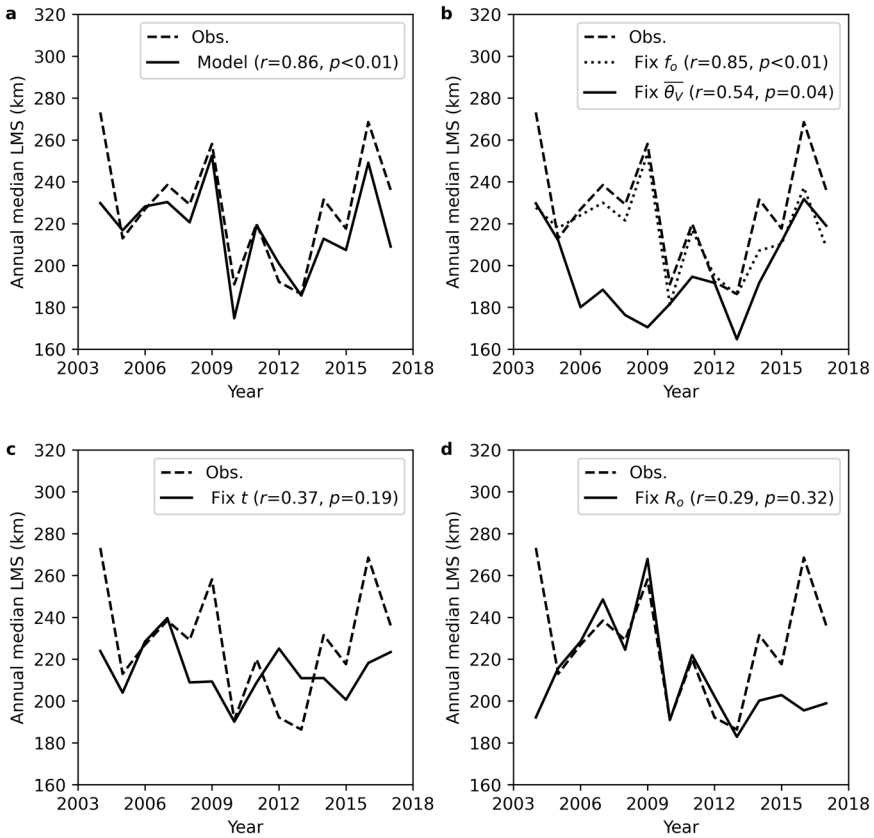

Fig. 5 Global annual LMS. The LMS of each TC is modeled by Eq. (9) with full variables in (**a**), fixed f_o or $\overline{\alpha_V}$ in (**b**), fixed t in (**c**), and fixed R_o in (**d**). If f_o, $\overline{\alpha_V}$, t or R_o is fixed, the median values of 4.2×10^{-5} s^{-1}, 0.9°, 90 h or 83 km is used, respectively. The Pearson correlation coefficient (r) of the detrended observed and modeled time series are given in the figure legend.

the growth model (Eq. (7)), the growth process is only terminated when the radial inflow ceases. Applying the model to a decrease of R_{34} would require radial outflow at the top of the boundary layer by, for example, the Ekman spin down due to the surface turbulent drag[51,52].

The growth model sheds light on the principal drivers of the interannual variation of LMS. The global LMS variability has so far been primarily driven by the variability in the duration of the growth. Future duration and hence LMS could change by, for example, a change in track length and/or change in translation speed. Predictions of translation speed are not uniform[53,54] so it is not clear what the likely changes of LMS could be.

Several studies have shown that the TC size has a positively skewed distribution for the radius of the outermost closed isobar[10], the radius of 15 m s^{-1} wind[11], the radius of 17 m s^{-1} wind[55], and the radius of the eye[14]. A previous study[37] shows explicitly that the radius of vanishing storm wind is log-normally distributed when normalized by a relevant TC length scale defined as the ratio of the potential intensity to the Coriolis parameter. It has also been shown that the global distribution of the radius of 12 m s^{-1} is approximately lognormal only after the same normalization[12].

In our analysis, the LMS of NA and EP TCs both follow a lognormal distribution without any normalization. This is not contradictory to the previous study[12] since their size climatology covered all sizes during a lifecycle. We show that the initial size distribution does not show a significant lognormal feature, but the lognormality of LMS is asymptotically achieved via exponential growth. Why does exponential growth increase the lognormality of the variable?

The exponential growth model is essentially an expression of the law of proportionate effect that states that according to the Central Limit Theorem, a lognormal distribution will be generated in the asymptotic limit[56]. The accumulation of the proportionate effect through the exponential growth process enhances the lognormal feature of the variate[57], and in our analysis, this variate is the TC outer size.

The main uncertainty of the current study comes from the best-track data set taken from the National Hurricane Center (NHC) and Joint Typhoon Warming Center (JTWC). Consensus methods[58] are used at both NHC and JTWC for operational R_{34} forecast. Most of our analysis is based on the NHC best track in the NA and EP after 2004 when the quality can be relatively more guaranteed after rigorous post-season analysis with more observations and proxies. In the NHC best track, the percentage uncertainty of R_{34} in the NA relative to the average value varies from about 25–35% depending on the availability of multiple observations[59]. The EP TC best track from NHC is also post-season quality controlled, but the associated uncertainty is unknown. Most of the R_{34} from the JTWC best track used in this study is real-time estimated since the post-season quality control only started at JTWC basins about three years ago. It was reported that the average R_{34} in the JTWC basins increases by 25% after the post-season analysis[60]. The mean R_{34} uncertainty from both NHC and JTWC has been estimated [61] to be about 15%. This uncertainty can be expected to be further reduced in the future[62].

An analytic growth model of TC outer size is derived in this study. The proposed model suggests an exponential process for the outer size growth. The observed composite of size growth shows a strong super linear nature, which supports the exponential growth of TC outer size. The analytic growth model can capture the size growth of both modeled and observed individual storm events. A climatology of TC size growth in the NA and EP for 2004–2017 identifies the key factors of size growth as

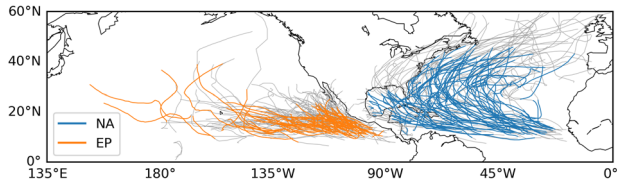

Fig. 6 TC tracks. Best track of NA and EP TCs for 2004–2017 before (gray tracks) and after (color tracks) data filtering.

suggested by the analytic growth model, i.e., the initial size, growth duration, mean growth latitude and mean effective inflow angle. These four variables are significantly different between NA and EP TCs. The lifetime maximum size distribution is lognormal, whereas the lognormal characteristic is much weaker for the initial size. It is the law of proportionate effect, a consequence of the exponential growth model, that enhances the lognormality of TC outer size via an exponential growth process.

A global climatology of TC size growth shows that each basin has a unique combination of size growth factors. The model framework presented here links together several previous empirical findings, such as the role of initial size on final size, the dependence of size on latitude, inter-basin size differences, and the lognormal distribution of size. The proposed growth model provides a simple framework to understand the interannual variability of the lifetime maximum size that may be largely driven by the variation of the growth duration.

METHODS

Data

The TC best-track data for 2004–2017, including the storm type (e.g., tropical storm, extratropical transition), geographical location, intensity, and R_{34} measurement, are taken from the International Best Track and Archive for Climate Stewardship[63] Version 4. In the NA and EP, the quality of R_{34} observations since 2004 can be relatively more guaranteed after rigorous post-season analysis[46], but we will also give a brief global climatology of TC size growth to cover the Western Pacific (WP), North Indian Ocean (NI), South Indian Ocean (SI) and South Pacific (SP). The TC best track in the NA and EP are taken from the National Hurricane Center (NHC), and for the other basins from the Joint Typhoon Warming Center (JTWC, Sampson et al.[60]).

The TC records in IBTrACS are reported regularly at 0000, 0600, 1200, and 1800 UTC. More frequent measurements during landfall are excluded from our analyses. For each best-track subset of individual cyclones, R_{34} is calculated as the mean in four quadrants. The quadrants where R_{34} equals 0 are excluded from the averaging following previous studies[64,65]. Figure 6 shows the full IBTrACS tracks (gray lines) in the NA and EP for 2004–2017. The partial tracks (color lines) used in our analysis are also highlighted in Fig. 6 after the following pre-processing procedures:

1. no extratropical transition period as labeled in the best-track data is considered,
2. a record is only considered if the TC center is over water,
3. only the records from the first R_{34} measurement to the lifetime maximum R_{34} are selected for each TC, and
4. TCs must have at least eight consecutive R_{34} records for 2 complete days.

Full-physics idealized tropical cyclone simulation

To validate the growth model and examine the steady-state inflow angle assumption we perform idealized TC simulations. We use the full-physics atmospheric Weather Research and Forecasting (WRF) Model[66] in the set-up described in ref. [20]. The run is configured with a triple nesting grid mesh, 4-km grid spacing in the innermost domain, and an initial bogus vortex specified with an analytic wind profile model[7,39]. The simulation is conducted in a stationary environment with a constant sea-surface temperature of 27 °C. The run lasts for 9 days, the last 6 days of which is employed for our analysis.

Lognormality test and statistical significance

The P value of a lognormal distribution test is estimated with the Kolmogorov–Smirnov (KS) test. The null hypothesis of the KS test is that the tested and target distributions are identical. A P value approaching unity indicates that the tested distribution becomes close to the target distribution. A bootstrapping method is applied to examine the statistical significance of the difference between two distributions, considering the skewness of the examined growth parameters. First, the two distributions are resampled 10,000 times to generate 10,000 pairs of distributions. Each resampled member has the same sample size as its parent distribution, and the elements in a parent distribution can be repeated during bootstrapping. Second, the difference in the means between the resampled distributions in each pair is calculated to form a new distribution with 10,000 samples. Thirdly, the percentile of zero difference is calculated to get the two-sided P value for the statistical significance. For example, a percentile of zero difference lower than the 2.5th or higher than the 97.5th suggests the two distributions are different at the 95% confidence interval.

Growth model fit

We validate the growth model (Eq. (9)) by fitting both simulated and observed TC outer size evolution with least-squares minimization. For each fit, there are six parameters: three inputs and three estimates. The three inputs are the observed: initial size, mean latitude during growth, and growth duration. Three estimates are made: the mean effective inflow angle $\overline{\alpha_V}$, LMS, and doubling time (Eq. (10)).

The R_{34} in the best track is measured by near-surface total wind speed, but the growth model is derived at the top of the boundary layer for a fixed tangential wind speed. To resolve this inconsistency, we assume a wind adjustment factor of 0.75 from the top of the boundary layer to surface[67,68]. We will fit the model to the surface R_{34}, but with this adjustment factor, the tangential wind of 34 kt at the surface R_{34} will be adjusted to 34/0.75 kt ≈45 kt at the top of the boundary layer. A vertical disconnection of lower-troposphere horizontal wind during landfall may happen[69], and that may significantly change the wind adjustment factor. However, that concern does not apply to our analysis since any landfall period is not included in our analysis. Our general results are not sensitive to the choice of the adjustment factor varying between 0.7 and 1.0.

DATA AVAILABILITY

Tropical cyclone best-track data can be downloaded from the National Centers for Environmental Information website (https://www.ncei.noaa.gov/data/international-best-track-archive-for-climate-stewardship-ibtracs/v04r00/access/csv/ibtracs.ALL.list.v04r00.csv).

CODE AVAILABILITY

The source codes for the analysis of this study are available from the corresponding author upon reasonable request.

Received: 9 November 2021; Accepted: 13 May 2022;
Published online: 09 June 2022

REFERENCES

1. Kantha, L. Time to replace the Saffir-Simpson Hurricane scale? *Eos, Transact. Am. Geophys. Union* **87**, 3 (2006).
2. Powell, M. & Reinhold, T. A. Tropical cyclone destructive potential by integrated kinetic energy. *Bull. Am. Meteorol. Soc.* **88**, 513–526 (2007).
3. Zhai, A. R. & Jiang, J. H. Dependence of US Hurricane economic loss on maximum wind speed and storm size. *Environ. Res. Lett.* **9**, 1–9 (2014).
4. Done, J. M., PaiMazumder, D., Towler, E. & Kishtawal, C. M. Estimating impacts of North Atlantic tropical cyclones using an index of damage potential. *Clim. Change* http://link.springer.com/10.1007/s10584-015-1513-0 (2015).
5. Irish, J. L., Resio, D. T. & Ratcliff, J. J. The influence of storm size on hurricane surge. *J. Phys. Oceanography* **38**, 2003–2013 (2008).
6. Lin, N., Lane, P., Emanuel, K. A., Sullivan, R. M. & Donnelly, J. P. Heightened hurricane surge risk in northwest Florida revealed from climatological-hydrodynamic modeling and paleorecord reconstruction. *J. Geophys. Res.* **119**, 8606–8623 (2014).

7. Wang, S. & Toumi, R. On the relationship between hurricane cost and the integrated wind profile. *Environ. Res. Lett.* **11**, 114005 (2016).
8. Wang, S. & Toumi, R. A historical analysis of the mature stage of tropical cyclones. *Int. J. Climatol.* **38**, 2490–2505 (2018).
9. Wang, S. & Toumi, R. Reduced sensitivity of tropical cyclone intensity and size to sea surface temperature in a radiative-convective equilibrium environment. *Adv. Atmos. Sci.* **35**, 981–993 (2018).
10. Merrill, R. T. A comparison of large and small tropical cyclones. *Monthly Weather Rev.* **112**, 1408–1418 (1984).
11. Liu, K. S. & Chan, J. C. L. Size of tropical cyclones as inferred from ERS-1 and ERS-2 data. *Monthly Weather Rev.* **127**, 2992–3001 (1999).
12. Chavas, D. R. & Emanuel, K. A. A QuikSCAT climatology of tropical cyclone size. *Geophys. Res. Lett.* **37**, L18816 (2010).
13. Chan, K. T. F. & Chan, J. C. L. Global climatology of tropical cyclone size as inferred from QuikSCAT data. *Int. J. Climatol.* **35**, 4843–4848 (2015).
14. Kimball, S. K. & Mulekar, M. S. A 15-year climatology of North Atlantic tropical cyclones. Part I: size parameters. *J. Clim.* **17**, 3555–3575 (2004).
15. Depperman, C. E. Notes on the origin and structure of Philippine typhoons. *Bull. Amer. Meteor. Soc* **28**, 399–404 (1947).
16. Holland, G. J. An analytic model of the wind and pressure profiles in Hurricanes. *Monthly Weather Rev.* **108**, 1212–1218 (1980).
17. Chavas, D. R., Lin, N. & Emanuel, K. A model for the complete radial structure of the tropical cyclone wind field. Part I: comparison with observed structure. *J. Atmos. Sci.* **72**, 3647–3662 (2015).
18. Chan, K. T. F. & Chan, J. C. L. Angular momentum transports and synoptic flow patterns associated with tropical cyclone size change. *Monthly Weather Rev.* **141**, 3985–4007 (2013).
19. Hill, K. A. & Lackmann, G. M. Influence of environmental humidity on tropical cyclone size. *Monthly Weather Rev.* **137**, 3294–3315 (2009).
20. Wang, S. & Toumi, R. Impact of dry midlevel air on the tropical cyclone outer circulation. *J. Atmos. Sci.* **76**, 1809–1826 (2019).
21. Bruneau, N., Wang, S. & Toumi, R. Long memory impact of ocean mesoscale temperature anomalies on tropical cyclone size. *Geophys. Res. Lett.* **47**, 1–19 (2020).
22. Ma, C. et al. Effects of background state on tropical cyclone size over the Western North Pacific and Northern Atlantic. *Clim. Dyn.* **52**, 4143–4156 (2019).
23. Chavas, D. R. & Lin, N. A model for the complete radial structure of the tropical cyclone wind field. Part II: wind field variability. *J. Atmos. Sci.* **73**, 3093–3113 (2016).
24. Cocks, S. B. & Gray, W. M. Variability of the outer wind profiles of western North Pacific typhoons: classifications and techniques for analysis and forecasting. *Monthly Weather Rev.* **130**, 1989–2005 (2002).
25. Kilroy, G., Smith, R. K. & Montgomery, M. T. Why do model tropical cyclones grow progressively in size and decay in intensity after reaching maturity? *J. Atmos. Sci.* **73**, 467–503 (2016).
26. Knaff, J. A., Longmore, S. P. & Molenar, D. A. An objective satellite-based tropical cyclone size climatology. *J. Clim.* **27**, 455–476 (2014).
27. Schenkel, B. A. et al. Lifetime evolution of outer tropical cyclone size and structure as diagnosed from reanalysis and climate model data. *J. Clim.* **31**, 7985–8004 (2018).
28. Zhang, J. A., Rogers, R. F., Nolan, D. S. & Marks, F. D. On the characteristic height scales of the hurricane boundary layer. *Monthly Weather Rev.* **139**, 2523–2535 (2011).
29. Willoughby, H. E. Gradient balance in tropical cyclones. *J. Atmos. Sci.* **47**, 265–274 (1990).
30. Li, Y., Wang, Y., Lin, Y. & Wang, X. Why does rapid contraction of the radius of maximum wind precede rapid intensification in tropical cyclones? *J. Atmos. Sci.* **78**, 3441–3453 (2021).
31. Holland, G. J., Belanger, J. I. & Fritz, A. A revised model for radial profiles of Hurricane winds. *Monthly Weather Rev.* **138**, 4393–4401 (2010).
32. Chavas, D. R. & Reed, K. A. Dynamical aquaplanet experiments with uniform thermal forcing: system dynamics and implications for tropical cyclone genesis and size. *J. Atmos. Sci.* **76**, 2257–2274 (2019).
33. DeMaria, M. A simplified dynamical system for tropical cyclone intensity prediction. *Monthly Weather Rev.* **137**, 68–82 (2009).
34. Emanuel, K. A fast intensity simulator for tropical cyclone risk analysis. *Natural Hazards* **88**, 779–796 (2017).
35. Wang, S. & Toumi, R. On the intensity decay of tropical cyclones before landfall. *Sci. Rep.* **12**, 1–8 (2022).
36. Rotunno, R. & Emanuel, K. An air-sea interaction theory for tropical cyclones. Part2: evolutionary study using a nonhydrostatic axisymmetric numerical model. *J. Atmos. Sci.* **44**, 542–561 (1987).
37. Dean, L., Emanuel, K. A. & Chavas, D. R. On the size distribution of Atlantic tropical cyclones. *Geophys. Res. Lett.* **36**, https://doi.org/10.1029/2009GL039051 (2009).
38. Chan, K. T. F. & Chan, J. C. L. Impacts of initial vortex size and planetary vorticity on tropical cyclone size. *Quarterly J. Royal Meteorol. Soc.* **140**, 2235–2248 (2014).
39. Wang, S., Toumi, R., Czaja, A. & Kan, A. V. An analytic model of tropical cyclone wind profiles. *Quarterly J. Royal Meteorol. Soc.* **141**, 3018–3029 (2015).
40. Wang, S., Rashid, T., Throp, H. & Toumi, R. A Shortening of the life cycle of major tropical cyclones. *Geophys. Res. Lett.* **47**, https://doi.org/10.1029/2020GL088589 (2020).
41. Lavender, S. L. & McBride, J. L. Global climatology of rainfall rates and lifetime accumulated rainfall in tropical cyclones: influence of cyclone basin, cyclone intensity and cyclone size. *Int. J. Climatol.* **41**, 1–19 (2021).
42. Wang, S. & Toumi, R. Recent tropical cyclone changes inferred from ocean surface temperature cold wakes. *Sci. Rep.* **11**, 22269 (2021).
43. Kossin, J. P., Emanuel, K. A. & Vecchi, G. A. The poleward migration of the location of tropical cyclone maximum intensity. *Nature* **509**, 349–352 (2014).
44. Zhang, J. A. & Uhlhorn, E. W. Hurricane sea surface inflow angle and an observation-based parametric model. *Monthly Weather Rev.* **140**, 3587–3605 (2012).
45. Maclay, K. S., DeMaria, M. & Vonder Haar, T. H. Tropical cyclone inner-core kinetic energy evolution. *Monthly Weather Rev.* **136**, 4882–4898 (2008).
46. Knaff, J. A., Sampson, C. R. & Chirokova, G. A global statistical-dynamical tropical cyclone wind radii forecast scheme. *Weather Forecasting* **32**, 629–644 (2017).
47. Xu, J. & Wang, Y. Sensitivity of the simulated tropical cyclone inner-core size to the initial vortex size. *Monthly Weather Rev.* **138**, 4135–4157 (2010).
48. Kilroy, G. & Smith, R. K. The effects of initial vortex size on tropical cyclogenesis and intensification. *Quarterly J. Royal Meteorol. Soc.* **143**, 2832–2845 (2017).
49. Musgrave, K. D., Taft, R. K., Vigh, J. L., McNoldy, B. D. & Schubert, W. H. Time evolution of the intensity and size of tropical cyclones. *J. Adv. Modeling Earth Syst.* **4**, n/a–n/a (2012).
50. Martinez, J., Nam, C. C. & Bell, M. M. On the contributions of incipient vortex circulation and environmental moisture to tropical cyclone expansion. *J. Geophys. Res.: Atmos.* **125**, 1–26 (2020).
51. Eliassen, A. & Lystad, M. The Ekman layer of a circular vortex-A numerical and theoretical study. *Geophysica Norvegica* **31**, 1–16 (1977).
52. Montgomery, M. T., Snell, H. D. & Yang, Z. Axisymmetric spindown dynamics of Hurricane-like vortices. *J. Atmos. Sci.* **58**, 421–435 (2001).
53. Kossin, J. P. A global slowdown of tropical-cyclone translation speed. *Nature* **558**, 104–107 (2018).
54. Yamaguchi, M., Chan, J. C., Moon, I. J., Yoshida, K. & Mizuta, R. Global warming changes tropical cyclone translation speed. *Nat. Commun.* **11**, 1–7 (2020).
55. Chan, K. T. F. & Chan, J. C. L. Size and strength of tropical cyclones as inferred from QuikSCAT data. *Monthly Weather Rev.* **140**, 811–824 (2012).
56. Limpert, E., Stahel, W. A. & Abbt, M. Log-normal distributions across the sciences: keys and clues. *BioScience* **51**, 341 (2001).
57. Aitchison, J. & Brown, J. A. C. *The Lognormal Distribution with Special Reference to Its Uses in Economics* (Cambridge Univ. Press, 1957).
58. Sampson, C. R. et al. Tropical cyclone gale wind radii estimates, forecasts, and error forecasts for the western North Pacific. *Weather Forecasting* **33**, 1081–1092 (2018).
59. Landsea, C. W. & Franklin, J. L. Atlantic Hurricane database uncertainty and presentation of a new database format. *Monthly Weather Rev.* **141**, 3576–3592 (2013).
60. Sampson, C. R. et al. Tropical cyclone gale wind radii estimates for the western North Pacific. *Weather Forecasting* **32**, 1029–1040 (2017).
61. Combot, C. et al. Extensive high-resolution synthetic aperture radar (SAR) data analysis of tropical cyclones: comparisons with SFMR flights and best track. *Monthly Weather Rev.* **148**, 4545–4563 (2020).
62. Knaff, J. A. et al. Estimating tropical cyclone surface winds: current status, emerging technologies, historical evolution, and a look to the future. *Tropical Cyclone Res. Rev.* **10**, 125–150 (2021).
63. Knapp, K. R., Kruk, M. C., Levinson, D. H., Diamond, H. J. & Neumann, C. J. The international best track archive for climate stewardship (IBTrACS). *Bull. Am. Meteorol. Soc.* **91**, 363–376 (2010).
64. Demuth, J. L., DeMaria, M. & Knaff, J. A. Improvement of advanced microwave sounding unit tropical cyclone intensity and size estimation algorithms. *J. Appl. Meteorol. Climatol.* **45**, 1573–1581 (2006).
65. Carrasco, C. A., Landsea, C. W. & Lin, Y.-L. The influence of tropical cyclone size on its intensification. *Weather Forecasting* **29**, 582–590 (2014).
66. Skamarock, W. C. et al. A description of the advanced research WRF version 3 (No. NCAR/TN-475+ STR), University Corporation for Atmospheric Research. National Center for Atmospheric Research Boulder, Colorado, USA, https://doi.org/10.5065/D68S4MVH (2008).
67. Franklin, J. L., Black, M. L. & Valde, K. GPS dropwindsonde wind profiles in hurricanes and their operational implications. *Weather Forecasting* **18**, 32–44 (2003).
68. Kepert, J. & Wang, Y. The dynamics of boundary layer jets within the tropical cyclone core. Part II: nonlinear enhancement. *J. Atmos. Sci.* **58**, 2485–2501 (2001).
69. Chen, J. & Chavas, D. R. The transient responses of an axisymmetric tropical cyclone to instantaneous surface roughening and drying. *J. Atmos. Sci.* **77**, 2807–2834 (2020).

70. Rozoff, C. M., Nolan, D. S., Kossin, J. P., Zhang, F. & Fang, J. The roles of an expanding wind field and inertial stability in tropical cyclone secondary eyewall formation. *J. Atmos. Sci.* **69**, 2621–2643 (2012).

ACKNOWLEDGEMENTS

This work was supported by the Natural Environment Research Council/UKRI (NE/V017756/1) and the UK-China Research and Innovation Partnership Fund through the Met Office Climate Science for Service Partnership (CSSP) China as part of the Newton Fund.

AUTHOR CONTRIBUTIONS

S.W. and R.T. conceived the study. S.W. analyzed the results. S.W. completed the draft and both authors reviewed the manuscript.

COMPETING INTERESTS

The authors declare no competing interests.

ADDITIONAL INFORMATION

Correspondence and requests for materials should be addressed to Shuai Wang.

Reprints and permission information is available at http://www.nature.com/reprints

Publisher's note Springer Nature remains neutral with regard to jurisdictional claims in published maps and institutional affiliations.